BRAIN CONNECTIVITY
Volume 3, Number 1, 2013

DOI: 10.1089/brain.2012.0114

Magnetic Resonance Field Strength Effects on Diffusion Measures and Brain Connectivity Networks

Liang Zhan,[1] Bryon A. Mueller,[2] Neda Jahanshad,[1] Yan Jin,[1] Christophe Lenglet,[3] Essa Yacoub,[3] Guillermo Sapiro,[4] Kamil Ugurbil,[3] Noam Harel,[3] Arthur W. Toga,[1] Kelvin O. Lim,[2] and Paul M. Thompson[1,5]

Abstract

The quest to map brain connectivity is being pursued worldwide using diffusion imaging, among other techniques. Even so, we know little about how brain connectivity measures depend on the magnetic field strength of the scanner. To investigate this, we scanned 10 healthy subjects at 7 and 3 tesla—using 128-gradient high-angular resolution diffusion imaging. For each subject and scan, whole-brain tractography was used to estimate connectivity between 113 cortical and subcortical regions. We examined how scanner field strength affects (i) the signal-to-noise ratio (SNR) of the non-diffusion-sensitized reference images (b_0); (ii) diffusion tensor imaging (DTI)-derived fractional anisotropy (FA), mean, radial, and axial diffusivity (MD/RD/AD), in atlas-defined regions; (iii) whole-brain tractography; (iv) the 113×113 brain connectivity maps; and (v) five commonly used network topology measures. We also assessed effects of the multi-channel reconstruction methods (sum-of-squares, SOS, at 7T; adaptive recombine, AC, at 3T). At 7T with SOS, the b_0 images had 18.3% higher SNR than with 3T-AC. FA was similar for most regions of interest (ROIs) derived from an online DTI atlas (ICBM81), but higher at 7T in the cerebral peduncle and internal capsule. MD, AD, and RD were lower at 7T for most ROIs. The apparent fiber density between some subcortical regions was greater at 7T-SOS than 3T-AC, with a consistent connection pattern overall. Suggesting the need for caution, the recovered brain network was apparently more efficient at 7T, which cannot be biologically true as the same subjects were assessed. Care is needed when comparing network measures across studies, and when interpreting apparently discrepant findings.

Key words: brain network analysis; DTI; fractional anisotropy; graph theory; high-field MRI; high angular resolution diffusion imaging (HARDI); signal-to-noise ratio; tractography

Introduction

Diffusion-weighted magnetic resonance imaging (DW-MRI) is a powerful and non-invasive technique to study white matter microstructure. It can be used to compute a wide array of measures of fiber connectivity and integrity in the brain. Several ongoing international efforts are mapping brain connectivity in populations of thousands of subjects; these include the Human Connectome Project based primarily in the United States (www.humanconnectomeproject.org), the IMAGEN project based in Europe (Whelan et al., 2012), and the 1000 Functional Connectomes Project (www.nitrc.org/projects/fcon_1000/), among many others. Other efforts have begun to map structural and functional brain connectivity with diffusion MRI in children and adolescents (Dennis et al., 2012a; Thomason et al., 2011), and in patient populations with Alzheimer's disease (Nir et al., 2012), or in groups of subjects carrying risk genes for disorders such as autism (Dennis et al., 2012b).

Much of the effort to map brain networks has focused on DW-MRI and its extensions, which can map axonal pathways and tracts in the living brain. Diffusion MRI is sensitive to the local direction and rate of water diffusion at each location in the brain. Axonal pathways may be reconstructed using tractography methods to infer the most likely paths of tracts, using computations based on the diffusion tensor imaging (DTI) or higher-order (e.g., *q*-space) diffusion models (Aganj et al., 2011; Jones, 2008; Leow et al., 2009a; Tuch, 2004; Wedeen et al., 2012).

Other methods exist to map functional connectivity, although the meaning of connectivity is different—for example, in resting-state fMRI, and magnetoencephalography/electroencephalography, temporal correlations are measured

[1]Imaging Genetics Center, Laboratory of Neuro Imaging, Department of Neurology, UCLA School of Medicine, Los Angeles, California.
[2]Department of Psychiatry, University of Minnesota, Minneapolis, Minnesota.
[3]Center for Magnetic Resonance Research, University of Minnesota, Minneapolis, Minnesota.
[4]Department of Electrical and Computer Engineering, Duke University, Durham, North Carolina.
[5]Department of Psychiatry, UCLA School of Medicine, Los Angeles, California.

between signals at pairs of locations in the brain. Diffusion-based connectivity mapping has broad applications in neurology and psychiatry for understanding disrupted patterns of brain connections, for example, in Alzheimer's disease (Nir et al., 2012), autism (Dennis et al., 2012b), and childhood neurogenetic disorders, as well as sex differences, hemispheric differences, and genetic effects on connectivity (Daianu et al., 2012; Duarte-Carvajalino et al., 2012; Jahanshad et al., 2011, 2012).

Some recent technical innovations in tracking fibers focus on *q*-space imaging, which enriches the local information available on directional diffusion. The quest to improve the local diffusion reconstruction has led to elaborate *q*-space sampling schemes with large numbers of directional samples (High Angular Resolution Diffusion Imaging), and/or multiple diffusion weightings (*b*-values). With multiple diffusion weightings, one can detect non-monoexponential radial diffusion, tracking different populations of diffusing water molecules in different cellular compartments—trapped within axons or moving more freely (Assaf and Basser, 2005; Kamath et al., 2012; Ozarslan et al., 2006; Wedeen et al., 2005; Zhan et al., 2011).

In basic diffusion models, diffusion properties are considered to not depend strongly on the static magnetic field strength of the scanner. For example, in the Stejskal-Tanner model of magnetic resonance (MR) signal decay (Stejskal and Tanner, 1965), the signal attenuation due to diffusion, in the (unit vector) direction g_k, is modeled as $S_k/S_0 = exp[-bg_k^T D g_k]$. Here, S_0 is the MR signal in the non-diffusion-weighted reference image(s); b is a diffusion-weighting factor containing information on the pulse sequence, gradient strength, and physical constants; and D is the three-dimensional diffusion tensor. Here, the strength of the static polarizing magnetic field (B_0)* does not directly influence the recovered diffusion measurements. Nevertheless, at higher magnetic fields, the signal-to-noise ratio (SNR) for DWI-derived measures is generally higher (Polders et al., 2011). However, high-field scans may also be more prone to certain types of artifacts, including distortions due to eddy currents, magnetic susceptibility gradients at tissue interfaces (e.g., in frontal and temporal sinuses), and chemical shift artifacts. Inhomogeneities in the B_0 field (Gross et al., 2006) may offset SNR advantages by increasing image distortion, blurring, or signal loss. Increases in the specific absorption rate and in the B_1 inhomogeneities can also limit the practical high field SNR advantages. Thus, the use of higher performing gradients, optimized B_0 shimming, and multi-channel RF coil technology is imperative to make diffusion imaging work at high fields. With appropriate technical solutions to the high-field problems, however, greater SNR can be realized at high fields, permitting the use of smaller voxels that reduce partial volume effects (PVE). PVE—from multiple tissue types or fiber directions in the same voxel—can confound accurate modeling of the diffusion signal, affecting apparent diffusion anisotropy and dominant directions (Leow et al., 2009b; Zhan et al., 2009a,b).

All these factors influence the accuracy of the final diffusion measures (Choi et al., 2011). Several empirical and theoretical studies show how signal to noise in diffusion MRI data depends on the spatial and angular resolution (Landman et al., 2007; Jahanshad et al., 2010; Zhan et al., 2010). Other studies optimize the *q*-space sampling to boost SNR in clinically feasible scan times (Zhan et al., 2012). Much less attention has been devoted to understanding how brain networks constructed from tractography, as well as patterns of recovered connections, depend on the spatial resolution and field strength of the DW-MRI scans. Spatial resolution affects even the simplest DTI measures, such as fractional anisotropy (FA)—the most widely used measure of brain integrity. When larger voxels are used, FA measures can be greatly reduced by PVE (Zhan et al., 2012).

In this study, we collected data from 23 healthy adults to monitor how scanner field strength affects SNR, diffusion measures, and networks describing cortical and subcortical connectivity. For the first time, we assessed how connectivity networks depend on the field strength. We hypothesized that scanner field strength would affect standard measures of cortical and subcortical connectivity. We expected that some tracts (e.g., thinner tracts and some pathways with substantial fiber crossings) might only be successfully recovered at high field strength. Depending on the connections present, the apparent efficiency or topology of the network may differ, and we were interested in the anatomical scope and extent of these effects.

We note that this effort is partially related to work by Zalesky et al. (2010), assessing how measures of structural connectivity depend, to some extent, on the selection, number, and density of the regions of interest (ROI) (nodes) in the network. Empirical data on these questions will help us determine how well scan data may be pooled or compared in multi-site DWI studies; many such studies are underway or planned. Those designing DWI protocols may also be interested to know how comparable their brain connectivity maps are likely to be, relative to independently collected data from other imaging centers. Our goal was to identify connectivity measures that might be vulnerable to protocol differences as a target for a more focused study, or mathematical improvements to make them more robust to scanning protocols.

Materials and Methods

Subject demographics and image acquisition

Whole-brain anatomical and DW-MRIs at both 7 and 3 tesla were collected at the Center for Magnetic Resonance Research, University of Minnesota; the protocols and subject information are summarized in Table 1 (Stanisz et al., 2005; Yacoub et al., 2003). The standard head coils were used on both systems: the 12-channel receive-only array on the 3T, and the Nova 24 channel transmit/receive coil on the 7T. Three datasets were collected using 3T and 7T protocols that were consistent in many respects, including a fixed 2 mm isotropic voxel size. Two millimeter voxels were chosen as they are commonly used in many DTI studies; in other work, we have studied how DTI measures depend on the voxel size and number of gradients in the protocol (Zhan et al., 2012). At the time of the data acquisition, there were also unavoidable differences in the scanner hardware that would preclude a perfectly matched comparison of 3T and 7T. As a result, this article attempts to compare scanning protocols that have been equalized to the fullest possible extent,

*In this article and elsewhere, it is common to use B_0 to refer to the static (non-varying) component of the scanner magnetic field, but b_0 is used to refer to the diffusion weighting applied when collecting reference images—usually at or close to 0 sec/mm^2.

Table 1. Comparison of Key DW-MRI Scan Parameters for the 3 and 7 Tesla Scans

Protocol description					
MRI machine name				*Siemens TIM Trio 3T*	*Siemens Magnetom 7T*
PAT mode				GRAPPA	GRAPPA
Acceleration factor PE				2	2
Isotropic voxel size (mm)				2.0	2.0
TR/TE (ms)				7800/82	5700/57
FOV (mm)				192×192	256×256
Diffusion weighting, b (sec/mm^2)				1000	1000
Number of diffusion weighted images (DWI)				128	128
Number of non-diffusion weighted reference images (b_0 images)				15	15
Total scan time (seconds)				1138	832
Dataset 1 23 subjects	Age	23.75±2.62	Field strength	3T	7T
	Sex	11 female	Reconstruction method	AC	SOS
Dataset 2 9 subjects	Age	73.95±12.79	Field strength	3T	3T
	Sex	7 female	Reconstruction method	AC	SOS
Dataset 3 5 subjects	Age	78.35±9.39	Field strength	7T	7T
	Sex	5 female	Reconstruction method	SOS	SENSE1

All scan protocols used single-spin echo DTI sequences, to allow for shorter TE times. Other consistently applied sequence parameters included an acquisition of 64 slices, 2-mm isotropic voxels, a b-value of 1000 sec/mm^2, 128 diffusion directions and 15 $b=0$ scans. TE and TR times were set to be the fastest possible allowed by the system. The superior gradient performance of the 7T scanner allowed for significantly shorter TE and TR times than could be achieved at 3T.

DW-MRI, diffusion-weighted magnetic resonance imaging; SOS, sum-of-squares; AC, adaptive recombine; DTI, diffusion tensor imaging; TR, time to repetition; TE, time to echo.

while recognizing that some parameters will have different optimal values depending on the field strength and the scanner hardware. Clearly, these were optimized for the scanner in each case, as would be done in any practical situation on commercially available scanners, rather than deliberately limiting one scanner's performance to match the other. Where relevant, we have noted these below, and we include information on how much they are expected to affect the results. Specifically, the default multi-channel reconstruction method for the DWI data used on the 7T scanner was sum-of-squares (SOS), while the default reconstruction method on the 3T scanner was adaptive recombine (AC). To avoid confusion throughout the remainder of the article, we refer to the scans as 3T-AC and 7T-SOS, in cases where the distinction is helpful. Experiments were also conducted to investigate whether the signal reconstruction method contributed to the differences observed between the scanners. For one of the datasets we analyze (dataset 2, below), DWI data were acquired from a group of nine volunteers on the 3T system. The same raw DWI data were then reconstructed using both the AC and SOS algorithms, for direct comparison of the two reconstruction methods at 3T (we refer to these reconstructed datasets as 3T-AC and 3T-SOS). In yet another dataset (dataset 3), DTI data were acquired on the 7T scanner from a group of five volunteers and reconstructed using the SOS and SENSE1 algorithms (referred as 7T-SOS and 7T-SENSE1) (Pruessmann et al., 1999). The AC algorithm was not available on the 7T scanner at the time of this study, and the SENSE1 reconstruction algorithm uses a similar but superior method to the AC algorithm (Lenglet et al., 2012).

T1-weighted anatomical images were acquired at 3 tesla with the following acquisition parameters: GRAPPA mode; acceleration factor PE = 2; TI/time to repetition (TR)/time to echo (TE) = 1100/2530/3.65 ms; echo spacing = 8.5 ms; flip angle = 7°; slice thickness = 1.0 mm, with an acquisition matrix of 256×256. All scanning protocols were approved by the medical Institutional Review Boards of the University of Minnesota and of the UCLA School of Medicine, where the analyses were performed. All subjects gave informed consent after study protocols were explained.

Image preprocessing

All DWI data were visually inspected by an experienced rater for evidence of the known Siemens vibration dropout artifact (Gallichan et al., 2010). No dropout artifact was found in the DW data as was expected since the CMRR TIM Trio had undergone the Siemens hardware upgrade designed to fix this artifact, before data acquisition for this study. All raw DWI images were corrected, as far as possible, for distortions due to eddy currents and motion using the *eddy_correct* function from the FMRIB software library (FSL) toolbox (http://fsl.fmrib.ox.ac.uk/fsl) (Smith et al., 2004; Woolrich et al., 2009). Geometric distortions due to magnetic susceptibility were then corrected using a field map collected just before the DTI, using the FSL *prelude* and *fugue* functions. Non-brain regions were removed from a T2-weighted image (b_0) in the corrected DWI dataset using the *bet* function in FSL. A trained neuroanatomical expert manually edited the T2-weighted scans to refine the brain extraction and to ensure the same brain coverage among different field strength protocols. This step was important to avoid bias, as different connectivity patterns might be recovered if brain coverage is allowed to vary. All calculations and analyses below are based on this preprocessed dataset.

SNR and scalar comparison

Our main goal was to examine field strength effects on measures of brain connectivity, but first we compared the SNR of the non-diffusion-sensitized images (b_0) between 3

and 7 tesla, as well as ROI-based DTI-derived measures, including FA, mean diffusivity (MD), axial diffusivity (AD), and radial diffusivity (RD). The diffusion tensor was estimated in each subject's native space using the *dtifit* function in FSL, and this was used to compute all DTI measures; after that, each subject's FA map was registered to the online ICBM DTI-81 atlas (www.loni.ucla.edu/ICBM/) (Mori et al., 2005) using the *flirt* function in FSL; subsequently, a non-linear refinement of this registration was performed using the *fnirt* function in FSL. The DTI atlas orientation and correctness of the anatomical labels were carefully checked. The resulting deformation field was applied to each subject's MD, AD, RD, and b_0 images using *applywarp* in FSL. This process was repeated for all datasets in Table 1. No major visual differences were observed between protocols in each dataset. All DTI-derived measures were compared using the 15 ROIs from the ICBM atlas (Table 4). In the meantime, a small ROI, referred to as the SNR-ROI, was manually defined in the mid-sagittal corpus callosum (CC) on the ICBM DTI-81 atlas, to assess SNR in a small and relatively homogeneous region. SNR was estimated as in the section *Motion evaluation and SNR comparison*.

Brain connectivity computation

We computed tractography and cortical networks in the native space of the data, after the preprocessing steps in the section *Image preprocessing*. Whole-brain DTI tractography (Wang et al., 2007) was initiated in regions for which FA $\geq$ 0.2; paths were stopped when they reached a region with FA $<$ 0.2; they were also stopped if the fiber direction encountered a sharp turn (where the critical angle threshold $\geq$ 30°). Sharp right-angle turns may be biologically possible in some cases (Wedeen et al., 2012), but allowing right-angle turns in tractography would create large numbers of false-positive pathways at fiber crossings. The Diffusion Toolkit (http://trackvis.org/dtk/) (Wang et al., 2007) uses these parameters to generate 3D fiber tracts, using the Orientation Distribution Function model, computed using the 2nd-order Runge-Kutta method (Basser et al., 2000). We used all voxels (with FA $\geq$ 0.2) as seed voxels to generate the fibers. After that, a spline filter was applied to each generated fiber, with units expressed in terms of the minimum voxel size of the dataset. Each subject's dataset contained 25,000–40,000 useable fibers (3D curves). All duplicate fibers and very short fibers (shorter than 10 mm) were removed.

Cortical and subcortical ROIs were defined using the Harvard Oxford Cortical and Subcortical probabilistic atlases (Desikan et al., 2006). Midline cortical masks were bisected into left and right components, to define separate hemispheric ROIs for each cortical region. Since this is a probabilistic atlas, the masks were set to a liberal threshold of 10% to include tissue along the gray–white matter interface, where fiber orientation mapping and tractography are most reliable (Morgan et al., 2009). To register these ROIs to each subject's DTI space, we used FSL's *flirt* function to determine the optimal affine transformation between the MNI152 T1 average brain (in which the Harvard Oxford probabilistic atlases are based) and each subject's unique FA image. We used a 12 degree-of-freedom registration with a mutual information cost function. We applied the resulting transformation to register the 113 ROIs to each subject's DTI space. To ensure that ROI masks did not overlap with each other after registration, each voxel was uniquely assigned to the mask for which it had the highest probability of membership. Table 2 lists all the ROIs.

For each pair of ROIs, the number of fibers connecting them was determined from the tractography results. A fiber was considered to connect two ROIs if it intersected both ROIs. This process was repeated for all ROI pairs, to compute a whole brain fiber connectivity matrix. This matrix is symmetric, by definition, and has a zero diagonal (no self-connections). Figure 1 shows a flow chart of steps involved in computing brain connectivity matrices.

On the 113 $\times$ 113 matrices generated above, we used the popular Brain Connectivity Toolbox (https://sites.google.com/site/bctnet/) (Rubinov and Sporns, 2010) to compute five standard graph theory measures, including *Characteristic Path Length* (CPL), *Global Efficiency* (GE), *Mean Clustering Coefficient* (MCC), *Modularity* (MOD), and *the degree of small-worldness* (SW), for each protocol in each dataset (Table 1) that describe organizational properties of each person's network.

CPL measures network integration by averaging the shortest path lengths between all pairs of nodes (Watts and Strogatz, 1998). GE is defined as the sum of the inverses of the shortest distances between each pair of nodes. Both lower GE values and longer CPL values are considered to indicate less efficient networks although whether or not they are functionally less efficient is conjectural without relevant functional data (Achard and Bullmore, 2007). The clustering coefficient measures the degree to which nodes in a graph tend to cluster together. Nodes with high clustering coefficient form locally interconnected clusters. MCC is the average of the local clustering coefficient of all nodes. MOD reflects the degree of natural segregation within a network (Newman, 2006), and can help to identify functional blocks within it. Given two parcellations into distinct modules for the same network, the one with the higher MOD value may have denser connections between the nodes within modules, but sparser connections between nodes in different modules. Furthermore, networks with the small-world property have been theorized to exhibit an optimal balance between functional integration and local clustering. Mathematically, SW is calculated as a ratio of local clustering and CPL of a node relative to the same ratio in a randomized network with globally equivalent edges/densities/strengths (Maslov and Sneppen, 2002). About 100 simulated random networks were generated for this study. A small-world network is demonstrated by an SW greater than 1, indicating a higher level of clustering for a similar CPL, compared to a randomly generated network. The equations to calculate each of these measures can be found in Rubinov and Sporns (2010).

Results

Motion evaluation and SNR comparison

Subject motion during the DWI acquisition was estimated using the *eddy_correct* function from the FSL toolbox. Each DWI was linearly registered to the first b_0 image; the per volume displacement was defined as $\mathrm{TR} = \sqrt{\mathrm{TR}_x^2 + \mathrm{TR}_y^2 + \mathrm{TR}_z^2}$, where TR_x, TR_y, and TR_z denote the corresponding translational distances, derived from the registration transform, in the x, y, and z directions, respectively (Jiang et al., 1995). The mean TR across all the diffusion images was then

Table 2. 113 Cortical and Sub-Cortical ROIs, Defined Using the Harvard Oxford Cortical and Subcortical Probabilistic Atlases (Desikan et al., 2006), Were Extracted as the Basis for Our 113×113 Connectivity Matrices

1,9	Thalamus	2,10	Caudate
3,11	Putamen	4,12	Pallidum
5	Brainstem	6,13	Hippocampus
7,14	Amygdala	8,15	Accumbens
16,17	Frontal pole	18,19	Insular cortex
20,21	Superior frontal gyrus	22,23	Middle frontal gyrus
24,25	Inferior frontal gyrus, pars triangularis	26,27	Inferior frontal gyrus, *pars opercularis*
28,29	Precentral gyrus	30,31	Temporal pole
32,33	Superior temporal gyrus, anterior division	34,35	Superior temporal gyrus, posterior division
36,37	Middle temporal gyrus, anterior division	38,39	Middle temporal gyrus, posterior division
40,41	Middle temporal gyrus, temporooccipital part	42,43	Inferior temporal gyrus, anterior division
44,45	Inferior temporal gyrus, posterior division	46,47	Inferior temporal gyrus, temporooccipital part
48,49	Postcentral gyrus	50,51	Superior parietal lobule
52,53	Supramarginal gyrus, anterior division	54,55	Supramarginal gyrus, posterior division
58,59	Lateral occipital cortex, superior division	60,61	Lateral occipital cortex, inferior division
56,57	Angular gyrus	62,63	Intracalcarine cortex
64,65	Frontal medial cortex	66,67	Juxtapositional lobule cortex
68,69	Subcallosal cortex	70,71	Paracingulate gyrus
72,73	Cingulate gyrus, anterior division	74,75	Cingulate gyrus, posterior division
76,77	Precuneus cortex	78,79	Cuneal cortex
80,81	Frontal orbital cortex	86,87	Lingual gyrus
82,83	Parahippocampal gyrus, anterior division	84,85	Parahippocampal gyrus, posterior division
88,89	Temporal fusiform cortex, anterior division	90,91	Temporal fusiform cortex, posterior division
92,93	Temporal occipital fusiform cortex	94,95	Occipital fusiform cortex
96,97	Frontal opercular cortex	98,99	Central opercular cortex
100,101	Parietal opercular cortex	102,103	*Planum polare*
104,105	Heschl's gyrus	106,107	*Planum temporale*
108,109	Supracalcarine cortex	110,111	Occipital pole
112,113	Cerebellum		

There are two numbers for each ROI in this table: the smaller number indicates the left side and large number denotes the right side. For example, "1" means the left thalamus, and "9" means the right thalamus.

ROI, regions of interest.

computed. As Dataset 2 (3T-AC vs. 3T-SOS) and Dataset 3 (7T-SOS vs. 7T-SENSE1) represent comparisons of reconstruction algorithms from the same raw data, there are no actual motion differences between the pairs of scans for a given subject in this dataset. Dataset 1, however, is a comparison of the same subjects, scanned on different scanners. The mean subject motion was 2.45 ± 0.89 mm for 3T-AC and 3.44 ± 0.64 mm for the 7T-SOS. The amount of motion was lower for the 3T-AC than the 7T-SOS ($p < 10^{-4}$; paired t test). This result is slightly surprising, as the 3T acquisition was 50% longer than the 7T acquisition, and it is not expected that a person would remain more still during a longer acquisition. One possible explanation is that the 7T scanner is less comfortable than the 3T scanner, which may lead to more motion (Gallichan et al., 2010). Note that since motion correction is applied to the images during the eddy current correction step, no confound is expected to affect the analysis.

Next, SNR was estimated from the b_0 images by (i) computing the voxel-wise mean and standard deviation (SD) in the SNR-ROI from all 15 corrected b_0 images for a given subject and scan type, and then (ii) subtracting the mean b_0 image from 15 individual b_0 images to create 15 residual images. The SNR was defined as the ratio of the grand mean and grand SD in the ROI from those residual images. SNR results for our three datasets are summarized in Table 3. Field dependence of image SNR in moving to 7T was examined rigorously both by electrodynamics calculations and through experimental measurements, using identical coil geometries and circuitry, and taking into account parameters such as the noise levels and coil efficiencies of the different systems (Vaughan et al., 2001). The SNR values measured here, however, include the T2 decays due to the use of spin echo in DWI and different TRs, and are not corrected for the different coils and instrument characteristics, as discussed previously. Empirically, we found that in dataset 1, the SNR was on average 18.3% higher for the 7T-SOS data than in 3T-AC data collected from the exact same subjects ($p = 0.016$, paired t-test; $\alpha = 0.05$; $n = 23$ subjects) even though the total scan time for the 3T scan was 36.8% longer than the scan time on the 7T. In datasets 2 and 3, whose purpose was to pick up any differences due to the reconstruction method, no significant difference was detected in the SNR between the different reconstruction methods. Although we cannot rule out that larger datasets may detect an effect of the reconstruction method, we can at least say that for these protocols the higher field strength (7T) likely contributes to the significant improvement in SNR. We note that the main effect of the different reconstruction methods is on the DWI not b_0, and is only likely to be strong at higher b-values (e.g., 3000 sec/mm^2; Lenglet et al., 2012).

Fiber integrity comparison

We conducted a Student's paired t-test on the ROI-based DTI-derived measures (FA, MD, AD, and RD) in 15 white matter ROIs (Table 4). To adjust for the number of paired

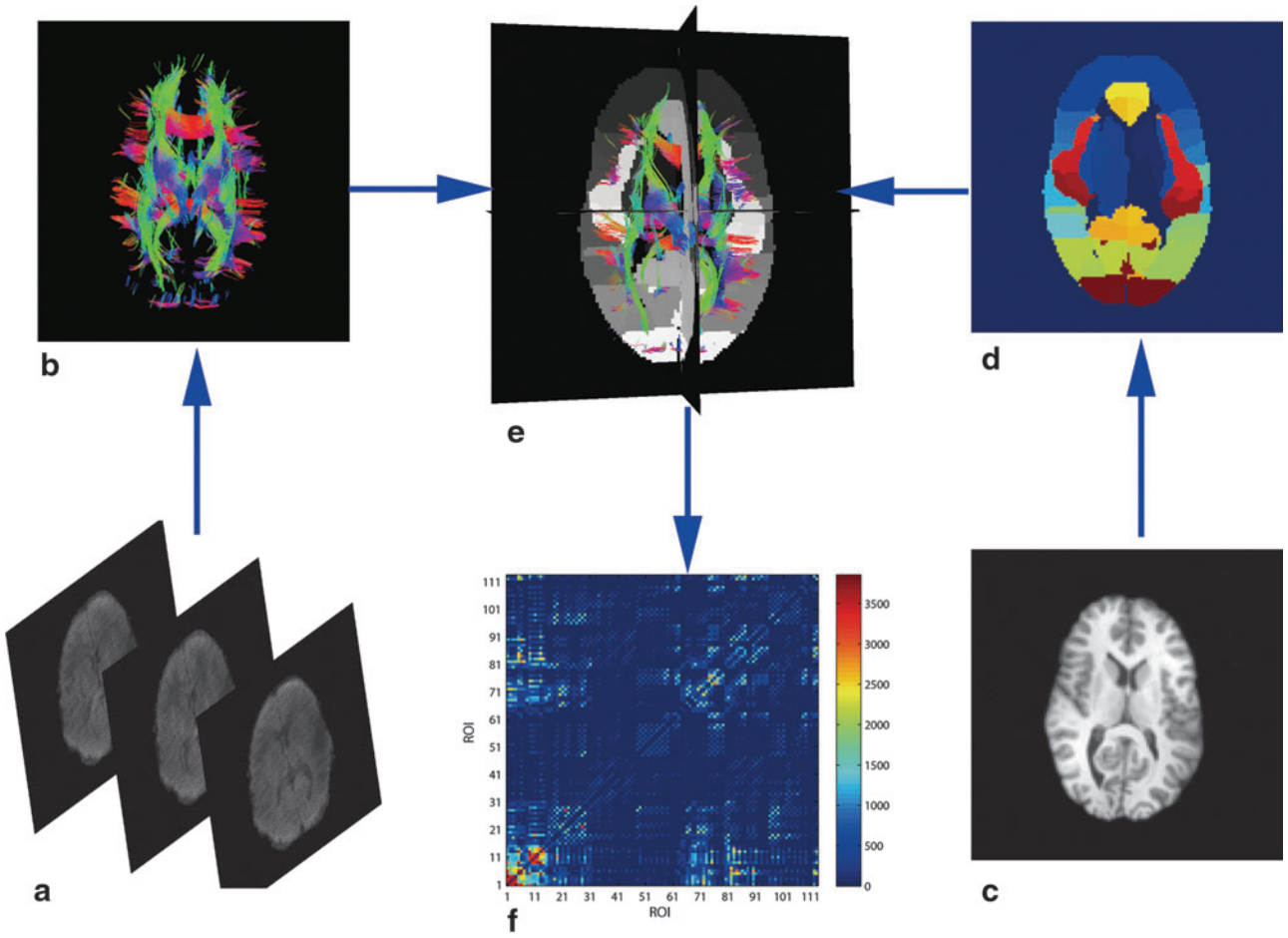

FIG. 1. Flowchart of steps to compute brain connectivity. Diffusion weighted images **(a)** are used as the basis to compute maps of whole-brain tractography **(b)**; in parallel, the standard T1-weighted anatomical magnetic resonance image from the same subject **(c)** is parcellated using the Harvard/Oxford Cortical and Subcortical probabilistic atlases, to define the regions of interest (ROIs) **(d)** by counting the number of detected fibers connecting each pair of ROIs **(e)**, and expressing them as a proportion of all fibers recovered in the entire brain, we can create the anatomical connectivity matrix **(f)**, for each subject in the study, and for each type of scan they had.

tests performed (i.e., 4 measures and 15 tests or each measure), the Bonferroni corrected significance threshold was set to $p < 0.05/60$, although this is arguably somewhat conservative as all the DTI-derived measures are quite highly correlated across subjects so they are not independent tests. All ROIs were defined in the refined ICBM DTI-81 atlas space. As previously mentioned, gray matter and CSF were removed by thresholding the FA maps, at FA ≥ 0.2. Each DTI-derived measure was averaged within the ROI and a paired *t*-test was conducted on all subjects in each dataset to assess systematic differences in this measure in each ROI, with respect to the scanning protocol used. Table 4 shows the mean DTI-derived measures (FA, MD, AD, and RD) for all ROIs for the comparison between 3T-AC and 7T-SOS. We compared the same 3T data reconstructed using the adaptive combine (3T-AC) and (3T-SOS) algorithm, and we compared the same

Table 3. SNR Differences in Head-to-Head Protocol Comparisons

Dataset 1	3T-AC	7T-SOS	Paired T test p $SNR_{3T\text{-}AC} < SNR_{7T\text{-}SOS}$
	4.0829 ± 1.1647	4.8307 ± 1.5126	**0.0158**
Dataset 2	3T-AC	3T-SOS	Paired T test p $SNR_{3T\text{-}AC} < SNR_{3T\text{-}SOS}$
	4.0923 ± 1.5521	4.0954 ± 1.6011	0.5707
Dataset 3	7T-SOS	7T-SENSE1	Paired T test p $SNR_{7T\text{-}SOS} < SNR_{7T\text{-}SENSE1}$
	4.0783 ± 1.1242	4.0172 ± 0.9190	0.6412

We listed the mean SNR for two protocols in each dataset, and the p value was computed from the Student's paired T test. When this p value < 0.05 (e.g., 0.0158 for dataset 1), it means the SNR of 7T-SOS is significantly higher than the SNR of 3T-AC in dataset 1; there were no detectable differences between the two protocols in dataset 2 ($p = 0.57$) and dataset 3 ($p = 0.64$). These results suggest that the field strength is likely to play an important role in boosting the SNR. Mathematically, the different reconstruction methods should give rise to some differences in SNR, but our failure to detect an SNR difference in datasets 2 and 3 suggests that reconstruction methods alone do not explain the observed boost in SNR at the higher field strength. The bold values highlight comparisons that passed the significance threshold.

SNR, signal-to-noise ratio.

Table 4. Comparison of DTI-Derived Measures Between 3T-AC and 7T-SOS

ROI name	1. Corpus callosum	6. Posterior thalamic radiation	11. Superior longitudinal fasciculus
	2. Cerebellar peduncle	7. Sagittal *stratum*	12. Fronto-occipital fasciculus
	3. Cerebral peduncle	8. External capsule	13. Uncinate fasciculus
	4. Internal capsule	9. Cingulum	14. *Tapetum*
	5. *Corona radiata*	10. Fornix and *stria terminalis*	15. Whole brain white matter

ROI index	*Mean* FA_{3T}	*Mean* FA_{7T}	*Paired T test p* ($FA_{3T} < FA_{7T}$)	*Mean* $MD_{3T} \times 10^{-3}$ *sec/m²*	*Mean* $MD_{7T} \times 10^{-3}$ *sec/m²*	*Paired T test p* ($MD_{3T} > MD_{7T}$)
1	0.5992	0.6087	3.5E-03	0.8512	0.8041	2.1E-07
2	0.4643	0.4681	0.30488	0.8823	0.8145	2.7E-06
3	0.5782	0.6107	1.0E-04*	0.7859	0.7505	2.8E-04
4	0.5691	0.5945	5.4E-06*	0.6878	0.6351	1.7E-14
5	0.4498	0.4685	6.7E-03	0.7102	0.6669	5.1E-08
6	0.534	0.5533	7.4E-03	0.7904	0.7330	1.2E-09
7	0.5061	0.5098	0.3560	0.7935	0.7117	1.9E-11
8	0.3899	0.3909	0.4138	0.7036	0.6458	8.1E-12
9	0.413	0.4234	0.0734	0.7108	0.6689	9.0E-08
10	0.4722	0.4896	6.5E-03	0.9692	0.9063	2.8E-06
11	0.4461	0.4597	0.0458	0.6821	0.6425	1.4E-08
12	0.461	0.4655	0.2698	0.7268	0.6506	6.7E-16
13	0.402	0.4035	0.4358	0.7469	0.6736	1.0E-11
14	0.4351	0.4542	0.0238	1.1906	1.1703	0.2400
15	0.4974	0.515	0.105	0.7615	0.7048	8.9E-16

ROI index	*Mean* $AD_{3T} \times 10^{-3}$ *sec/m²*	*Mean* $AD_{7T} \times 10^{-3}$ *sec/m²*	*Paired T test p* ($AD_{3T} > AD_{7T}$)	*Mean* $RD_{3T} \times 10^{-3}$ *sec/m²*	*Mean* $RD_{7T} \times 10^{-3}$ *sec/m²*	*Paired T test p* ($RD_{3T} > RD_{7T}$)
1	1.4938	1.4402	2.9E-06	0.5300	0.4860	1.9E-05
2	1.3570	1.2565	3.9E-07	0.6449	0.5934	9.5E-05
3	1.3715	1.3316	0.0041	0.4932	0.4600	0.0012
4	1.1966	1.1264	1.8E-10	0.4333	0.3894	1.3E-11
5	1.0869	1.0336	6.3E-08	0.5219	0.4835	1.2E-05
6	1.3144	1.2406	3.3E-08	0.5285	0.4792	3.3E-07
7	1.2770	1.1448	7.2E-11	0.5518	0.4951	4.3E-07
8	1.0117	0.9335	1.3E-09	0.5495	0.5020	7.4E-12
9	1.0586	1.0016	2.4E-06	0.5369	0.5026	7.4E-06
10	1.4938	1.4210	4.7E-05	0.7068	0.6489	6.1E-06
11	1.0311	0.9792	9.6E-11	0.5077	0.4741	5.5E-05
12	1.1319	1.0146	2.2E-16	0.5243	0.4686	3.3E-10
13	1.0981	0.9887	1.1E-08	0.5712	0.5161	3.2E-10
14	1.7207	1.7198	0.4916	0.9255	0.8955	0.1116
15	1.2258	1.1524	1.6E-15	0.5294	0.4810	1.8E-10

Each DTI-derived measure (FA, MD, AD, and RD) was calculated and averaged for each ROI in each subject. A Student's paired *T*-test was conducted to identify protocol effects between the 7T-SOS and 3T-AC data. The Bonferroni corrected *p*-value ($0.05/60 \approx 8.3 \times 10^{-4}$) was used to determine if there was a significant difference between protocols. For FA, only the 3rd and 4th ROIs showed a significant difference (7T-SOS > 3T-AC) after Bonferroni correction. We therefore conclude that FA may depend on field strength for some parts of the brain, but a significant difference was not observed in the majority of the regions we assessed. However, significantly lower diffusivity measures (MD, AD, and RD) were observed in the 7T-SOS data compared to the 3T-AC data for most ROIs, with a couple of exceptions (the 14th for MD, the 3rd and 14th for AD and RD). An asterisk indicates that the comparison in that location has passed the Bonferroni corrected threshold.

FA, fractional anisotropy; MD, mean diffusivity; AD, axial diffusivity; RD, radial diffusivity.

7T data reconstructed using the 7T-SOS and 7T-SENSE1 algorithms, to assess the effect of the reconstruction method. The reconstruction method had no detectable effect on all DTI-derived measures, as the paired *t*-test *p*-value was larger than 0.05/60 for all ROIs in datasets 2 and 3 (results not shown).

For dataset 1, several ROIs (the 1st, 3rd, 4th, 5th, 6th, 10th, 11th, and 14th ROI in Table 4) have *p*-values < 0.05, but after correction for multiple comparisons, only the cerebral peduncle (the 3rd ROI) and internal capsule (the 4th ROI) showed significant differences in FA between two field strengths. In prior reports (Choi et al., 2011), no effect of field strength on FA was found between 3T and 7T scans for a variety of different ROIs (the body, genu and splenium of the CC, the posterior limb of the internal capsule, and in the subcortical white matter region overall). Our results are consistent with this: some of our ROIs overlap with those in Choi et al. (2011) and we only found a field strength effect on FA in a brain region not assessed by Choi *et al.* In other work, we have noticed that the effect in the cerebral peduncle may be due to somewhat higher geometric distortions at 7T, which can generate voxels with artificially very high FA.

Table 4 shows that mean MD, AD, and RD were, on average, significantly different between 3T-AC and 7T-SOS for almost all comparisons even after Bonferroni correction. This result is similar to a prior study that reported that the apparent diffusion coefficient (=3*MD) values for gray and white

matter were statistically significantly lower at 3.0 tesla compared to 1.5 tesla, while FA values were statistically significantly higher at 3.0 tesla compared to 1.5 tesla (Huisman et al., 2006), although our results are the first examination of eigenvalue-related DTI measures at ultra-high field strength (7T). Since no significant differences were detected in the other two comparisons (3T-AC vs. 3T-SOS and 7T-SOS vs. 7T-SENSE1) at the $p = 0.05/60$ level (results not shown), we can conclude that these DTI-derived measures may depend to some extent on the field strength.

Tractography comparison

Next, we compared tractography and the constructed cortical network between 3T and 7T to evaluate how field strength may affect brain connectivity computations. Table 5 compares three basic fiber parameters (including the number of fibers, and maximum and mean fiber length) for the whole brain tractography results, between protocols in each dataset. For dataset 1, the number of fibers and mean fiber length showed a nominal difference between 3T-AC and 7T-SOS using a lax significance threshold of 0.05 (paired *t*-tests, $p = 0.03$ and 0.04, respectively). However, if we correct for multiple comparisons, the Bonferroni corrected significance threshold should be set to $p < 0.05/3$, so none of these is significant. Table 5 shows no detectable effect of the reconstruction methods on our tractography results (paired *t*-tests, $p > 0.05$ for dataset 2 and 3).

To further show that there were no drastic differences at the gross anatomical level, Figure 2 shows one frontal view of the whole-brain tractography for one subject per dataset. On visual inspection, the main white matter fiber tracts have similar orientations between protocols in each dataset. To quantitatively assess differences in whole-brain tractography, we conducted a formal network analysis.

Brain connectivity comparison

When comparing connectivity maps, it is important to assess connections that are robust and found in a reasonable number of individual subjects. If all subjects had a nonzero value for the connection between any two ROIs, we treated this connection as valid; otherwise, it was treated as zero. This makes the computed networks more robust to errors in tractography—especially errors that do not occur repeatedly in many different subjects. The first three rows in Figure 3 show that the mean connectivity patterns were visually similar between protocols. To assess differences in connectivity between protocols in each dataset, we performed a paired Student's *t*-test for each connection between every pair of ROIs in Table 2, only when the connection was non-zero at both field strengths. In this situation, 4206 connections were evaluated (the total number of possible connections is $113 \times 112/2 = 6328$). The resultant false discovery rate (FDR) (Benjamini and Hochberg, 1995) critical value (threshold) that controlled the false discovery rate at 5% was $p = 8.83 \times 10^{-3}$; only 18 connections passed the FDR critical threshold when testing connections for which 7T-SOS > 3T-AC in dataset 1 (i.e., testing connections more prevalent at 7T-SOS) and no connections were found significant in dataset 2 and 3 or when comparing 3T-AC > 7T-SOS (i.e., no connections were consistently more prevalent at 3T-AC) in dataset 1. As such, there was a significant difference in the *overall* pattern between 3T-AC and 7T-SOS, even after correcting for the number of valid connections tested. The last row in Figure 3 shows connections that passed FDR when comparing 7T-SOS > 3T-AC. For several pairs of regions, a greater proportion of connections was recovered at 7T-SOS, such as those between the *cingulate gyrus* ROI and thalamus. Moreover, greater deep subcortical connectivity was apparent at 7T-SOS (see last row in Fig. 3). Table 6 lists all connections that

Table 5. Comparison of Whole-Brain Fiber Tractography Summary Parameters Between Scanning Protocols, Across Three Datasets

	Dataset 1		
	Fiber number	*Max fiber length*	*Mean fiber length*
3T-AC	34582 ± 2089	170.16 ± 18.11 mm	35.29 ± 2.38 mm
7T-SOS	35618 ± 2216	167.90 ± 15.63 mm	36.86 ± 2.56 mm
Paired T test *p* value (3T-AC < 7T-SOS)	**0.0333**	0.9349	**0.0411**
	Dataset 2		
	Fiber number	*Max fiber length*	*Mean fiber length*
3T-AC	30736 ± 4080	173.02 ± 20.94 mm	34.57 ± 2.49 mm
3T-SOS	30262 ± 4008	176.08 ± 21.98 mm	34.64 ± 2.58 mm
Paired T test *p* value (3T-AC < 3T-SOS)	0.5964	0.3831	0.4765
	Dataset 3		
	Fiber number	*Max fiber length*	*Mean fiber length*
7T-SOS	31513 ± 2867	161.19 ± 16.39 mm	31.94 ± 1.96 mm
7T-SENSE1	31907 ± 3416	170.04 ± 20.92 mm	31.93 ± 2.05 mm
Paired T test *p* value (7T-SOS < 7T-SENSE1)	0.1035	0.0841	0.5465

Results are averaged across the subjects in each dataset. The minimum fiber length was set to 10 mm for each. To correct for multiple comparisons, the Bonferroni corrected significance threshold was set to $p < 0.05/3$. All results are null if properly corrected for multiple comparisons. The bold values highlight comparisons that passed the significance threshold.

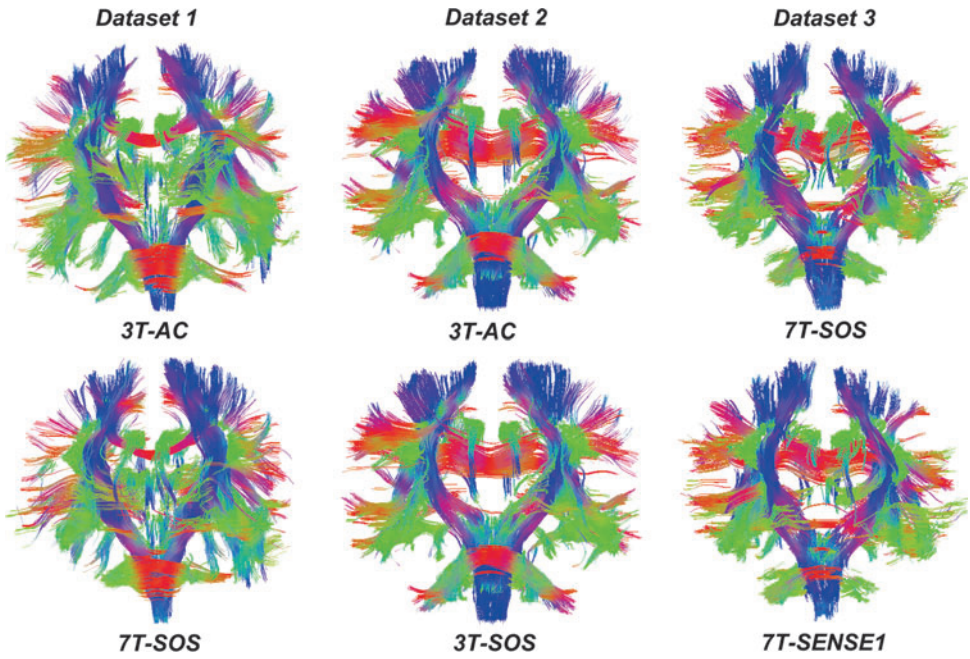

FIG. 2. Several coronal views allow a visual comparison of the whole-brain tractography results in one subject per dataset. They show generally similar gross anatomical patterns between protocols in each dataset. A color code is used to distinguish fibers with dominant diffusion directions in the left–right (*red*), anterior–posterior (*green*), and superior–inferior (*blue*) directions.

passed FDR, with their associated *p*-values. Although there must be an objective reality about the density of neural fibers in these regions, clearly the two protocols are differentially able to detect the connections in these regions, leading to a network representation that depends on the protocol. Moreover, Figure 3 also suggests that the difference in connectivity due to different reconstruction methods is not significant in our dataset, although it may be in others.

Field strength effects on network measures

We next tested how the choice of scanning protocol affected the five common network measures. One common step in graph theory analysis is to select a threshold for the network, termed the *sparsity*. Networks with a sparsity of 0.30 retain only 30% of the connections of the full-sparsity network, eliminating the ones with smallest weights (which tends to retain only the most reliable, major connections). We first computed five network measures at multiple levels of sparsity (over the allowable range, [0.01, 1], in increments of 0.01). Figure 4 shows that the general trends for five network measures between protocols in each dataset (listed in Table 1) are quite similar although there are differences in some sparsity measures. To compare these network measures, selecting a single sparsity level may arbitrarily affect the network measures; thus, we evaluated the area under the curve (AUC) over the selected range of sparsities to generate more stable scores for all network measures. The range selected is also an important factor for the evaluation, which is highly related to the specific network. We chose 0.21 as the lower boundary for the sparsity range, as it represents the point below which networks begin to fragment into multiple non-connected components, and therefore, the resultant graphs are considered to be unstable. This may be supported by the fluctuating curve in the range ([0.01 ~ 0.2]) in Figure 4. At higher sparsities, brain networks become topologically indistinguishable from random graphs and so are less biologically plausible (Sporns, 2011). To determine the upper boundary for the sparsity range, we calculated the network density for the unthresholded networks across all subjects—the lowest value was selected as it will still retain the most highly represented connections across all the subjects. So for each subject, the network density is calculated as the total number of edges in the raw brain network divided by the total number of possible connections in the network. 0.4527 was the smallest network density value for all the subjects, so we chose 0.45 as the upper limit of the sparsity range. We computed the AUC over the sparsity range [0.21, 0.45]; results of these comparisons are shown in Table 7.

From Table 7, the 7T-SOS protocol yielded networks, compared to 3T-AC, that had a significantly lower CPL, significantly higher GE and higher MCC, if we use the standard nominal significance threshold of $p < 0.05$. Clearly, they may be due to slight differences in the fiber counts and proportional representation of fibers between different regions, as well the detection of additional fibers. For other measures, there were no significant differences between 3T-AC and 7T-SOS. Furthermore, AUC comparisons of the five network measures by reconstruction method detected no effect of the reconstruction method when comparing 3T-AC with 3T-SOS, and when comparing 7T-SOS to 7T-SENSE1. Although the reconstruction methods may not have contributed significantly to the differences in network measures seen here, the network computed at a high field-strength (7T) *appears* to be more efficient than the corresponding one computed from a low field-strength (3T). Clearly, as the same subjects were assessed, there can be no biological reality to any claim that the network is more efficient when scanned in a certain way. More likely, the proportional representation of connections may cause these effects, as not all the connections in the brain can be imaged by any specific protocol. Even so, the MOD and SW metrics—two of the five most popular connectivity metrics used today—are more robust to scanner field strength than the others.

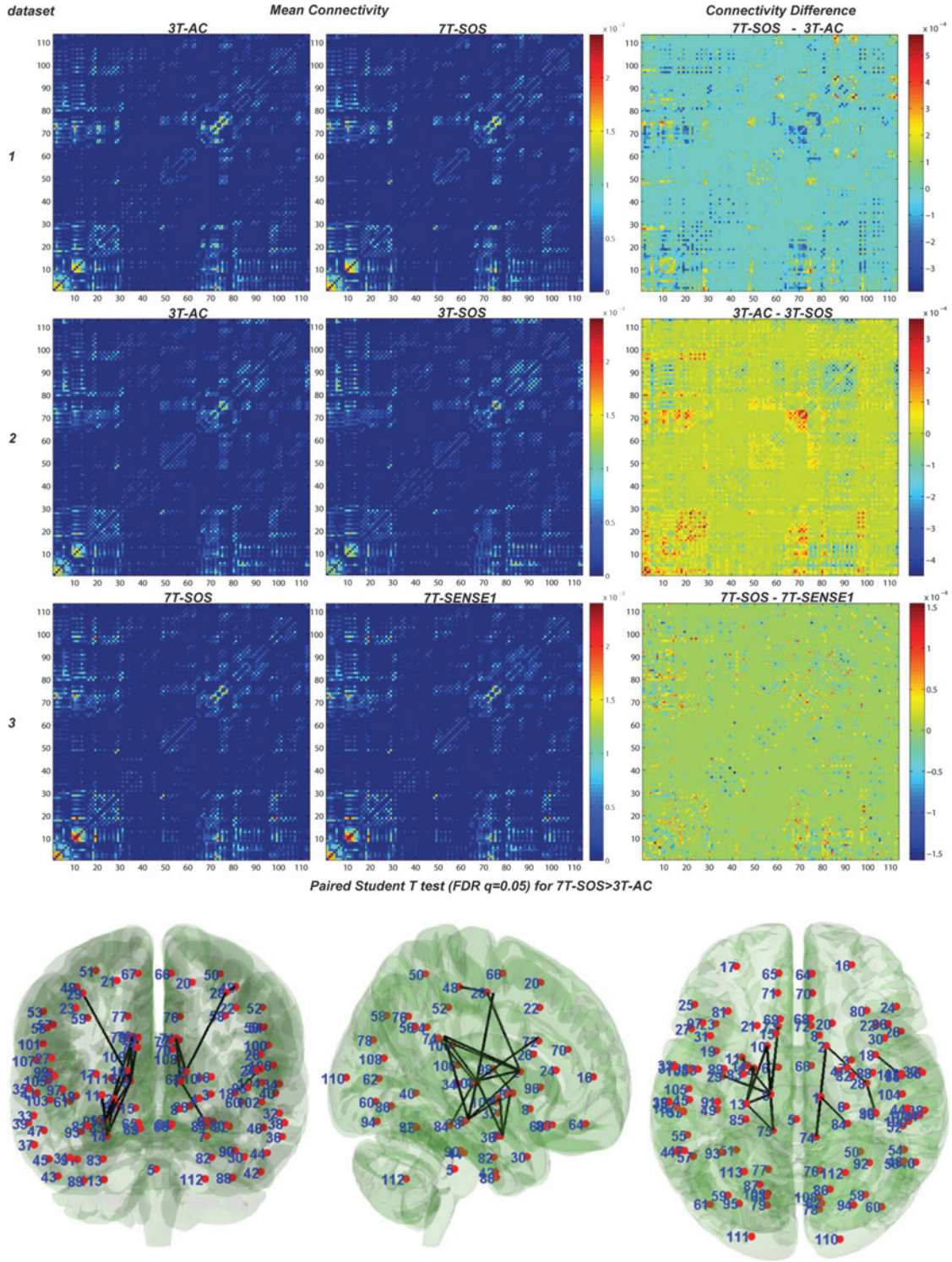

FIG. 3. Differences in measured brain connectivity patterns. The first three rows show the mean connectivity pattern (*first two columns*) and connectivity difference between protocols for the three datasets (in Table 1). Within each row, the exact same *subjects* are scanned—only the scanner or the reconstruction methods differ. All fiber counts are normalized to the whole brain fiber count, so this difference only refers to the proportional representation of connections, which leads to the assignment of weights in the overall network. In general, connectivity patterns are very similar across protocols. In the maps of mean connectivity across all subjects, red colors indicate a *stronger* connection (more fibers detected) and blue colors denote a weaker connection (fewer fibers); in the connectivity difference maps, a red color indicates a positive difference and a blue color represents a negative difference. The last row shows connections that passed false discovery rate (FDR) ($q=0.05$) in paired Student's *t*-tests when comparing 7T-SOS > 3T-AC in dataset 1 (i.e., connection density was higher at 7T-SOS). No connections passed FDR ($q=0.05$) in datasets 2 or 3—the tests of effects of reconstruction methods—or when comparing 3T-AC > 7T-SOS (i.e., where connection density was higher at 3T-AC) in dataset 1. Each red dot in the plot represents one ROI, numbered according to the index in Table 2. The line between two red dots represents the fiber connection between them (in reality, these are curved 3D lines, but a straight line is used for visual clarity). Overall, the higher field strength (7T) enhanced the apparent strength of some subcortical connections, that is, proportionally more fibers were detected in the whole brain tractography.

Table 6. Connections More Prominent at 7T

Connections	p *value*	*Connections*	p *value*
Right caudate and right thalamus	3.70E-03	Left postcentral gyrus and left precentral gyrus	1.02E-04
Right hippocampus and right thalamus	1.98E-04	Right cingulate gyrus, anterior division and right thalamus	1.10E-03
Right hippocampus and right caudate	6.51E-04	Left cingulate gyrus, posterior division and left thalamus	8.50E-03
Right hippocampus and right pallidum	3.50E-03	Left cingulate gyrus, posterior division and left caudate	3.80E-03
Right amygdala and right thalamus	8.80E-03	Right cingulate gyrus, posterior division and right thalamus	5.82E-05
Right amygdala and right putamen	7.90E-03	Right cingulate gyrus, posterior division and right caudate	1.93E-04
Right amygdala and right pallidum	8.50E-03	Right cingulate gyrus, posterior division and right hippocampus	1.20E-03
Left precentral gyrus and left caudate	7.77E-05	Left parahippocampal gyrus, posterior division and left thalamus	7.60E-03
Right precentral gyrus and right thalamus	1.80E-03	Left central opercular cortex and left insular cortex	2.0E-03

Here we list all the connections that passed the multiple comparisons threshold of FDR ($q = 0.05$), in paired Student's *t*-tests when comparing 7T-SOS > 3T-AC (i.e., connection density was higher at 7T-SOS) in dataset 1. This lists connections more prominent at 7T. FDR, false discovery rate.

Discussion and Conclusion

Our work here aimed to understand how higher field scanning (here 7T vs. 3T) might affect brain connectivity measures, including some of the main connectivity metrics used today. With the advent of major international efforts to examine brain connectivity both structurally and functionally, there is clear interest in understanding what factors affect fundamental brain connectivity metrics. These include scanner and protocol effects—not just biological effects. Such information is relevant when deciding how to pool connectivity data across scanners, and in deciding if changes in scanner protocols are likely to affect connectivity analyses.

In this study, the 7T and 3T scans differed in several respects. As expected from MRI theory, the higher field protocol boosted the SNR for some of the fundamental diffusion imaging parameters, such as the signal in the reference images (non-diffusion weighted images, or b_0 scans) collected to assess diffusion-based MR signal attenuation. This is a clear advantage as it boosts the SNR for all downstream computations (some more than others). Even so, the fiber integrity—as measured by the FA, a very widely used metric—was not systematically higher or lower at 7T for any studied ROI, or in the brain's white matter as a whole. This is also expected from MR theory. Two out of the 15 ROIs had nominally higher FA at 7T than 3T, but the effects were small and did not pass a multiple comparisons correction. However, MD, AD, and RD were significantly lower at 7T than 3T in most ROIs, an effect worthy of future study.

Connectivity matrices from whole-brain tractography tended to pick up a greater density for some subcortical connections at 7T, or—more precisely—there were several connections in the thalamus and hippocampus whose density was apparently higher at 7T. Clearly, there is a tendency to expect that the 7T data should better represent the objective reality of neural pathways. Nevertheless, without further validation, it is extremely difficult to say what the correct level of fiber representation is in a structural network. Clearly, it depends on the spatial scale of the measurement: in scans with larger voxels, thinner or less prominent connections will be overlooked, or de-emphasized. Ongoing work by Zalesky et al. (2010) examines how network nodes, weights, and properties depend on the selection of nodes, including how densely they are sampled. Parallel work by our own group revealed effects of voxel size, numbers of diffusion gradients, and diffusion weighting schemes on the local diffusion model. Any downstream operations, such as tractography and network measures, might show similar dependencies, as demonstrated here.

This study has limitations. With three datasets from two scanners, we were able to identify key differences in network patterns. However, we cannot say with certainty that other differences are not present. A larger sample of subjects would offer greater power to resolve differences, and this is one of the aims of the Human Connectome Project. We evaluated different data reconstruction methods that did not appear to affect the results.

A second unavoidable limitation is that the differences seen here may arise from differences in scanner capabilities, hardware, and sequence parameter choices, rather than differences that would be found on other 7T or at 3T scanners. Clearly, if we had used scanners with different capabilities (e.g., the 3T scanners to be used for the Human Connectome Project, which have maximum gradient strengths of 100 mT/m (Washington University–University of Minnesota Consortium) and 300 mT/m (MGH-UCLA consortium), or recently demonstrated accelerated pulse sequences that can reduce the repetition time (Feinberg et al., 2010; Setsompop et al., 2012), we may have found different patterns of differences, including the differences between scanners. A reasonable future goal might be to perform meta-analyses to see if the findings reported here are corroborated when much larger datasets are available.

Whether our observed network differences should cause concern for other studies depends on whether the biological

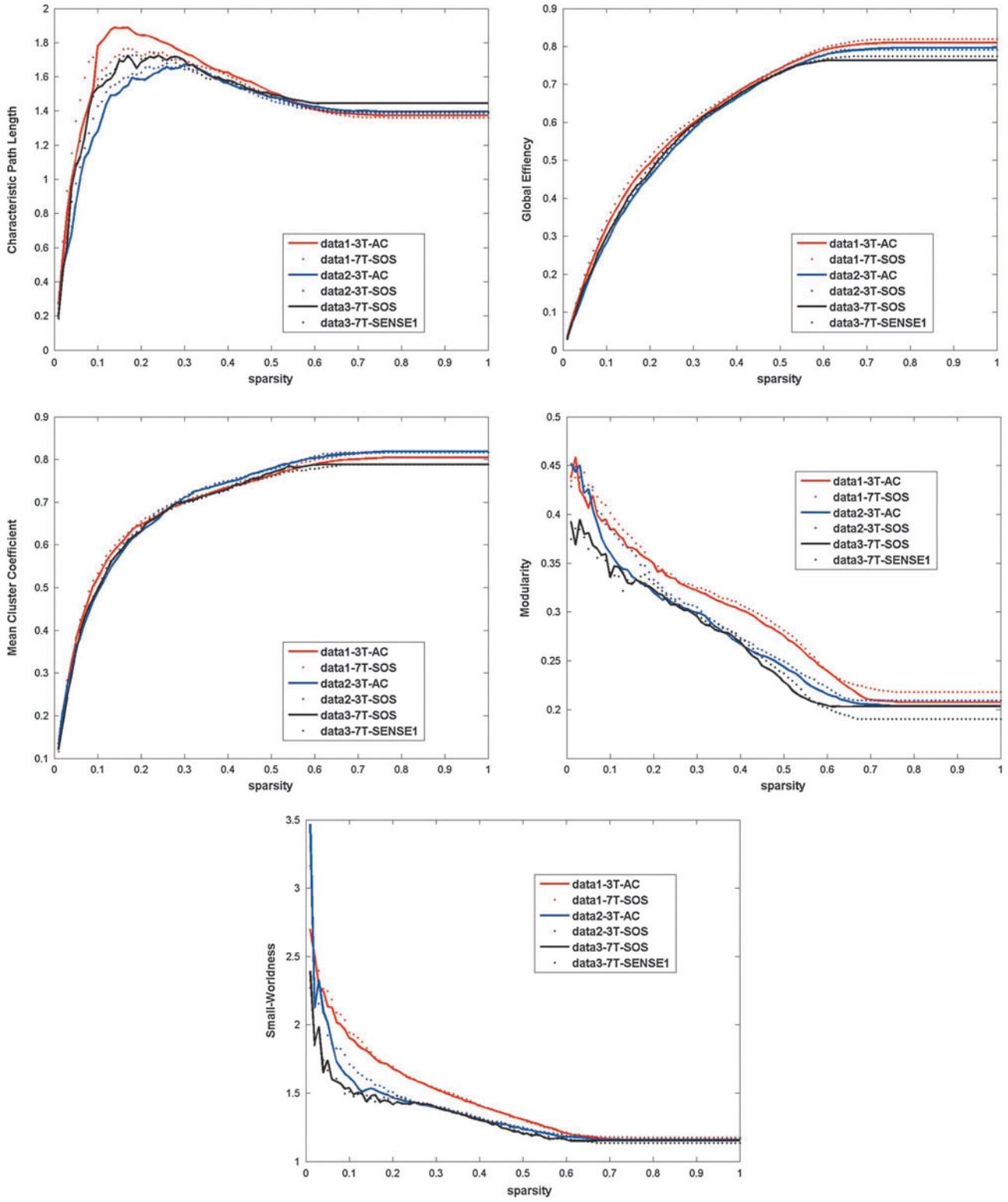

FIG. 4. Protocol effects on anatomical connectivity network measures, for our three datasets (Table 1). The general trends are similar, although there are differences at some sparsities. Sparsity is a free parameter in the comparison of networks, that controls what percentage of the edges are retained (here, we express it on a scale of 0.01 to 1; zero means an empty network and "1" means a full network).

Table 7. Scanning Protocol Effects on Commonly Used Summary Measures of Network Topology

Dataset 1	*3T-AC Mean AUC*	*7T-SOS Mean AUC*	*Paired T test* p *value*
CPL	42.7004	40.9354	**0.0033**
GE	15.2028	15.4454	**0.0095**
MCC	17.4921	17.7162	**0.0235**
MOD	7.8797	8.0401	0.2042
SW	37.7596	37.7813	0.4890
Dataset 2	*3T-AC Mean AUC*	*3T-SOS Mean AUC*	*Paired T test* p *value*
CPL	38.8022	39.5656	0.6812
GE	14.6296	14.7822	0.3159
MCC	17.5473	17.6579	0.3036
MOD	7.1473	7.3830	0.3419
SW	34.1526	34.6169	0.3881
Dataset 3	*7T-SOS Mean AUC*	*7T-SENSE1 Mean AUC*	*Paired T test* p *value*
CPL	40.3862	40.4778	0.5599
GE	14.8585	14.9692	0.2262
MCC	17.5064	17.4412	0.6272
MOD	7.0480	7.2272	0.3462
SW	33.5211	34.2680	0.3412

An area-under-the-curve (AUC) comparison is shown for five network measures in the sparsity range [0.21, 0.45] for dataset 1. The reason for comparing curves (and areas under those curves) is that the network measures depend on a sparsity parameter that determines how much of the network is retained. Therefore, the comparisons allow this to vary but aim to pick up any differences across the entire range of sparsities. We calculate the mean AUC across subjects and the p value is the probability computed from a Student's paired t-test for 3T-AC > 7T-SOS for CPL and 3T-AC < 7T-SOS for the rest of the four measures in dataset 1. Results indicated that in 7T-SOS in dataset 1, the lower CPL, higher GE, and higher MCC were significant, if we set the significance threshold as 0.05. If we correct for multiple comparisons, CPL and GE results are still significant. MOD and SW are most robust to scanner field strength. Furthermore, based on datasets 2 and 3, the reconstruction method does not lead to detectable differences in network measures. The bold values highlight comparisons that passed the significance threshold.

CPL, characteristic path length; GE, global efficiency; MCC, mean clustering coefficient; MOD, modularity; SW, small-worldness.

effects of interest are confounded with the scanner field strengths, whether the effects of interest are small relative to these scanner effects, and whether they can be adequately modeled or inferred. Sometimes, inter-scanner effects are a source of error variance that is not modeled at all. Clearly, as neural networks have a spatial scale finer than the resolution of current *in vivo* scanners, structural networks always do reflect scanner sensitivity to some extent. Some connections may be invisible, and some of those presented may be more robust than others. New mathematical metrics of network connectivity may also be developed in the future that are more robust to protocol and scanner effects, and their development may be spurred by empirical efforts to measure these effects. These may include meta-analytic methods, voting methods, and Bayesian methods, which have been successful in other fields.

Acknowledgments

This project was primarily funded by NIH R01 grants EB007813 and EB008432 to P.T., G.S., K.U., and K.L. from the NIBIB (additional support from this grant to C.L. and B.M. is also acknowledged). Although this collaborative project pre-dated the HCP initiative, K.U., N.H., G.S., C.L., and A.W.T. are also funded in part by the Human Connectome Project 1U54MH091657-01 from the 16 National Institutes of Health Institutes and Centers that support the NIH Blueprint for Neuroscience Research. The work is also supported by Biotechnology Research Center (BTRC) grant P41 RR008079 (NCRR)/P41 EB015894 (NIBIB).

Author Disclosure Statement

The authors have no competing financial interests.

References

Achard S, Bullmore E. 2007. Efficiency and cost of economical brain functional networks. PLoS Comput Biol 3:e17.

Aganj I, Lenglet C, Jahanshad N, Yacoub E, Harel N, Thompson PM, Sapiro G. 2011. A Hough transform global probabilistic approach to multiple-subject diffusion MRI tractography. Med Image Anal 15:414–425.

Assaf Y, Basser PJ. 2005. Composite hindered and restricted model of diffusion (CHARMED) MR imaging of the human brain. Neuroimage 27:48–58.

Basser PJ, Pajevic S, Pierpaoli C, Duda J, Aldroubi A. 2000. *In vivo* fiber tractography using DT-MRI data. Magn Reson Med 44:625–632.

Benjamini Y, Hochberg Y. 1995. Controlling the false discovery rate—a practical and powerful approach to multiple testing. J Roy Stat Soc B Met 57:289–300.

Choi S, Cunningham DT, Aguila F, Corrigan JD, Bogner J, Mysiw WJ, Knopp MV, Schmalbrock P. 2011. DTI at 7 and 3 T: systematic comparison of SNR and its influence on quantitative metrics. Magn Reson Imaging 29:739–751.

Daianu M, Jahanshad N, Dennis EL, Toga AW, McMahon KL, de Zubicaray GI, Wright MJ, Hickie I, Thompson PM. 2012. Left versus right hemisphere differences in brain connectivity: 4-Tesla HARDI tractography in 567 twins. ISBI 2012, Barcelona, Spain, May 2–5, 2012.

Dennis EL, Jahanshad N, Toga AW, Johnson K, McMahon KL, de Zubicaray GI, Montgomery G, Martin NG, Wright MJ,

Thompson PM. 2012a. Changes in anatomical brain connectivity between ages 12 and 30: a HARDI study of 484 adolescents and adults. ISBI 2012, Barcelona, Spain, May 2–5, 2012.

Dennis EL, Jahanshad N, Toga AW, Rudie JD, Dapretto M, Brown JA, Bookheimer SY, Johnson K, McMahon KL, de Zubicaray GI, Montgomery G, Martin NG, Wright MJ, Thompson PM. 2012b. Abnormal Structural Brain Connectivity in Healthy Carriers of the Autism Risk Gene, *CNTNAP2*, Brain Connectivity, published online, 2012.

Desikan RS, Ségonne F, Fischl B, Quinn BT, Dickerson BC, Blacker D, Buckner RL, Dale AM, Maguire RP, Hyman BT, Albert MS, Killiany RJ. 2006. An automated labeling system for subdividing the human cerebral cortex on MRI scans into gyral based regions of interest. Neuroimage 31:968–980.

Duarte-Carvajalino JM, Jahanshad N, Lenglet C, McMahon KL, de Zubicaray GI, Martin N, Wright M, Thompson PM, Sapiro G. 2012. Hierarchical topological network analysis of anatomical human brain connectivity and differences related to sex and kinship. Neuroimage 59:3784–3804.

Feinberg DA, Moeller S, Smith SM, Auerbach E, Ramanna S, Glasser MF, Miller KL, Ugurbil K, Yacoub E. 2010. Multiplexed echo planar imaging for sub-second whole brain FMRI and fast diffusion imaging. PLoS One 5:e15710.

Gallichan D, Scholz J, Bartsch A, Behrens TE, Robson MD, Miller KL. 2010. Addressing a systematic vibration artifact in diffusion-weighted MRI. Hum Brain Mapp 31:193–202.

Gross D, Zick K, Oerther T, Lehmann V, Pampel A, Goetz J. 2006. Hardware and methods. In: Stapf S, Han S-I (eds.) *NMR Imaging in Chemical Engineering*. Weinheim, FRG: Wiley-VCH Verlag GmbH & Co. KgaA.

Huisman TA, Loenneker T, Barta G, Bellemann ME, Hennig J, Fischer JE, Il'yasov KA. 2006. Quantitative diffusion tensor MR imaging of the brain: field strength related variance of apparent diffusion coefficient (ADC) and fractional anisotropy (FA) scalars. Eur Radiol 16:1651–1658.

Jahanshad N, Agani I, Lenglet C, Jin Y, Joshi A, Barysheva M, McMahon KL, de Zubicaray GI, Martin NG, Wright MJ, Toga AW, Sapiro G, Thompson PM. 2011. High angular resolution diffusion imaging (HARDI) Tractography in 234 young adults reveals greater frontal lobe connectivity in women, International Symposium on Biomedical Imaging: From Nano to Macro (ISBI) 2011; Springer, Chicago, IL, 939–943.

Jahanshad N, Kohannim O, Toga AW, McMahon KL, de Zubicaray GI, Martin NG, Wright MJ, Thompson PM. 2012. Diffusion imaging protocol effects on genetic associations. ISBI 2012, Barcelona, Spain, May 2–5, 2012.

Jahanshad N, Zhan L, Bernstein MA, Borowski BJ, Jack CR, Toga AW, Thompson PM. 2010. Diffusion tensor imaging in seven minutes: determining trade-offs between spatial and directional resolution. ISBI 2010, 1161–1164.

Jiang A, Kennedy DN, Baker JR, Weisskoff RM, Tootell RBH, Woods RP, Benson RR, Kwong KK, Brady TJ, Rosen BR, Belliveau JW. 1995. Motion detection and correction in functional MR imaging. Hum Brain Mapp 3:224–235.

Jones DK. 2008. Tractography gone wild: probabilistic fibre tracking using the wild bootstrap with diffusion tensor MRI. IEEE Trans Med Imaging 27:1268–1274.

Kamath A, Aganj I, Xu J, Yacoub E, Ugurbil K, Sapiro G, Lenglet C. 2012. Generalized Constant Solid Angle ODF and Optimal Acquisition Protocol for Fiber Orientation Mapping. MICCAI 2012 Workshop on Computational Diffusion MRI.

Landman BA, Farrell JAD, Jones CK, Smith SA, Prince JL, Mori S. 2007 Effects of diffusion weighting schemes on the reproducibility of DTI-derived fractional anisotropy, mean diffusivity, and principal eigenvector measurements at 1.5T. Neuroimage 36:1123–1138.

Lenglet C, Sotiropoulos S, Moeller S, Xu J, Auerbach EJ, Yacoub E, Feinberg D, Setsompop K, Wald L, Behrens TE, Ugurbil K. 2012. Multichannel Diffusion MR Image Reconstruction: How To Reduce Elevated Noise Floor And Improve Fiber Orientation Estimation. ISMRM Annual Meeting, Melbourne, Australia, May 2012.

Leow AD, Zhan L, Zhu S, Hageman N, Chiang MC, Barysheva M, Toga AW, Thompson PM. 2009b. White matter integrity measured by fractional anisotropy correlates poorly with actual individual fiber anisotropy. ISBI 2009, Boston, MA.

Leow AD, Zhu S, Zhan L, McMahon K, de Zubicaray GI, Meredith M, Wright M, Toga A, Thompson PM. 2009a. The tensor distribution function. Magn Reson Med 61:205–214.

Maslov S, Sneppen K. 2002. Specificity and stability in topology of protein networks. Science 296:910–913.

Morgan VL, Mishra A, Newton AT, Gore JC, Ding Z. 2009. Integrating functional and diffusion magnetic resonance imaging for analysis of structure-function relationship in the human language network. PLoS One 4:e6660.

Mori S, Wakana S, van Ziji PCM, Nagae-Poetscher LM. 2005. *MRI Atlas of Human White Matter*. Amsterdam, The Netherlands: Elsevier.

Newman MEJ. 2006. Modularity and community structure in networks. Proc Natl Acad Sci U S A 103:8577–8696.

Nir T, Jahanshad N, Jack CR, Weiner MW, Toga AW, Thompson PM, and the Alzheimer's Disease Neuroimaging Initiative (ADNI). 2012. Small world network measures predict white matter degeneration in patients with early-stage mild cognitive impairment. ISBI 2012, Barcelona, Spain, May 2–5, 2012.

Ozarslan E, Shepherd TM, Vemuri BC, Blackband SJ, Mareci TH. 2006. Resolution of complex tissue microarchitecture using the diffusion orientation transform (DOT). Neuroimage 31:1086–1103.

Polders DL, Leemans A, Hendrikse J, Donahue MJ, Luijten PR, Hoogduin JM. 2011. Signal to noise ratio and uncertainty in diffusion tensor imaging at 1.5, 3.0, and 7.0 Tesla. J Magn Reson Imaging 33:1456–1463.

Pruessmann KP, Weiger M, Scheidegger MB, Boesiger P. 1999 SENSE: Sensitivity encoding for fast MRI. Magn Reson Med 42:952–962.

Rubinov M, Sporns O. 2010. Complex network measures of brain connectivity: uses and interpretations. Neuroimage 52:1059–1069.

Setsompop K, Cohen-Adad J, Gagoski BA, Raij T, Yendiki A, Keil B, Wedeen VJ, Wald LL. 2012. Improving diffusion MRI using simultaneous multi-slice echo planar imaging. Neuroimage 63:569–580.

Smith SM, Jenkinson M, Woolrich MW, Beckmann CF, Behrens TEJ, Johansen-Berg H, Bannister PR, De Luca M, Drobnjak I, Flitney DE, Niazy R, Saunders J, Vickers J, Zhang Y, De Stefano N, Brady JM, Matthews PM. 2004. Advances in functional and structural MR image analysis and implementation as FSL. Neuroimage 23:208–219.

Sporns O. 2011. *Networks of the Brain.* Cambridge, MA: The MIT Press.

Stanisz GJ, Odrobina EE, Pun J, Escaravage M, Graham SJ, Bronskill MJ, Henkelman RM. 2005. T1, T2 relaxation and magnetization transfer in tissue at 3T. Magn Reson Med 54:507–512.

Stejskal EO, Tanner JE. 1965. Spin diffusion measurements: spin echoes in the presence of a time-dependent field gradient. J Chem Phys 42:288.

Thomason ME, Dennis EL, Joshi AA, Joshi SH, Dinov ID, Chang C, Henry ML, Johnson RF, Thompson PM, Toga AW, Glover GH, Van Horn JD, Gotlib IH. 2011. Resting-state fMRI can reliably map neural networks in children. Neuroimage 55:165–175.

Tuch DS. 2004. Q-Ball imaging. Magn Reson Med 52:1358–1372.

Vaughan JT, Garwood M, Collins CM, Liu W, DelaBarre L, Adriany G, Andersen P, Merkle H, Goebel R, Smith MB, Ugurbil K. 2001. 7T vs. 4T: RF power, homogeneity, and signal-to-noise comparison in head images. Magn Reson Med 46:24–30.

Wang R, Benner T, Sorensen AG, Wedeen VJ. 2007. Diffusion Toolkit: A Software Package for Diffusion Imaging Data Processing and Tractography. Proceedings of the International Society for Magnetic Resonance in Medicine, 15: p3720.

Watts DJ, Strogatz SH. 1998. Collective dynamics of 'small-world' networks. Nature 393:440–442.

Wedeen VJ, Hagmann P, Tseng WY, Reese TG, Weisskoff RM. 2005. Mapping complex tissue architecture with diffusion spectrum magnetic resonance imaging. Magn Reson Med 54:1377–1386.

Wedeen VJ, Rosene DL, Wang RP, Dai GP, Mortazavi F, Hagmann P, Kaas JH, Tseng WYI. 2012. The geometric structure of the brain fiber pathways. Science 335:1628–1634.

Whelan R, Conrod PJ, Poline JB, Lourdusamy A, Banaschewski T, et al. 2012. Adolescent impulsivity phenotypes characterized by distinct brain networks. Nat Neurosci 15:920–925.

Woolrich MW, Jbabdi S, Patenaude B, Chappell M, Makni S, Behrens T, Beckmann C, Jenkinson M, Smith SM. 2009. Bayesian analysis of neuroimaging data in FSL. Neuroimage 45:S173–S186.

Yacoub E, Duong TQ, Van De Moortele PF, Lindquist M, Adriany G, Kim SG, Uğurbil K, Hu X. 2003. Spin-echo fMRI in humans using high spatial resolutions and high magnetic fields. Magn Reson Med 49:655–664.

Zalesky A, Fornito A, Harding IH, Cocchi L, Yucel M, Pantelis C, et al. 2010. Whole-brain anatomical networks: does the choice of nodes matter? Neuroimage 50:970–983.

Zhan L, Jahanshad N, Ennis DB, Jin Y, Bernstein MA, Borowski BJ, Jack CR, Toga AW, Leow AD, Thompson PM. 2012. Angular versus spatial resolution trade-offs for diffusion imaging under time constraints. Hum Brain Mapp [Epub ahead of print]; DOI: 10.1002/hbm.22094

Zhan L, Leow AD, Aganj I, Lenglet C, Sapiro G, Yacoub E, Harel N, Toga AW, Thompson PM. 2011. Differential information content in staggered multiple shell HARDI measured by the tensor distribution function. ISBI 2011, 305–309.

Zhan L, Leow AD, Jahanshad N, Chiang MC, Barysheva M, Lee AD, Toga AW, McMahon KL, de Zubicaray GI, Wright MJ, Thompson PM. 2010. How does angular resolution affect diffusion imaging measures? Neuroimage 49:1357–1371.

Zhan L, Leow AD, Zhu S, Chiang MC, Barysheva M, Toga AW, McMahon KL, de Zubicaray GI, Wright MJ, Thompson PM. 2009a. Analyzing multi-fiber reconstruction in high angular resolution diffusion imaging using the tensor distribution function. ISBI 2009, Boston, MA.

Zhan L, Leow AD, Zhu S, Hageman N, Chiang MC, Barysheva M, Toga AW, Thompson PM. 2009b. What does Fractional Anisotropy (FA) really measure? Medical Image Computing and Computer Assisted Intervention (MICCAI 2009), London, UK.

Address correspondence to:
Paul Thompson
Laboratory of Neuro Imaging
Department of Neurology
UCLA School of Medicine
635 Charles Young Drive South, Suite 225
Los Angeles, CA 90095-7334

E-mail: thompson@loni.ucla.edu